Nanoscale

PAPER

View Article Online
View Journal | View Issue

Cite this: *Nanoscale*, 2023, **15**, 578

An intelligent, autocatalytic, DNAzyme biocircuit for amplified imaging of intracellular microRNAs†

Meirong Cui, Dan Zhang, Qingfu Wang and Jie Chao *

Received 20th September 2022,
Accepted 6th December 2022

DOI: 10.1039/d2nr05165f

rsc.li/nanoscale

DNAzymes hold great promise as transducing agents for the analysis of intracellular biomarkers. However, their low intracellular delivery efficiency and limited signal amplification capability (including an additional supply of cofactors) hinder their application in low-abundance biomarker analysis. Herein, a general strategy to design an intelligent, autocatalytic, DNAzyme biocircuit is developed for amplified microRNA imaging in living cells. The DNAzyme biocircuit is constructed based on a nanodevice composed of catalytic hairpin assembly (CHA) and DNAzyme biocatalytic functional units, sustained by Au nanoparticles (AuNPs) and MnO_2 nanosheets (CD/AM nanodevices). Once the CD/AM nanodevices are endocytosed by cells, the MnO_2 nanosheets are reduced by intracellular glutathione (GSH), which not only releases the different units of the DNAzyme circuit, but also generates the cofactor Mn^{2+} for DNAzyme autocatalysis. The intracellular analytes could trigger the coordinated cross-activation of CHA and autocatalytic DNAzymes on AuNPs, enabling reliable and accurate detection of miRNAs in living cells. This intelligent autocatalytic multilayer DNAzyme biocircuit can effectively avoid signal leakage and obtain high amplification gain, expanding the application of programmable complex DNA nanocircuits in biosensing, nanomaterial assembly, and biomedicine.

Introduction

Biochemical networks play important roles in material circulation, energy flow and information transmission in biological systems.[1] The coordination and connection between multiple biochemical networks ensure the normal operation of life activities.[2] The complex life network realizes the information transmission and regulation of different physiological functions through the up-regulation and down-regulation of specific biomolecules such as nucleic acids and proteins.[3,4] In this process, biochemical networks can recognize and sense a variety of important small molecules and execute specific programmed responses.[5–8] Simulating the molecular programs that make up biochemical networks and constructing biological circuits are critical for studying important biomolecules and related physiological activities in cells.[9–12] Previous works have reported that intelligently responsive nanomaterials and molecular circuits can be used to construct artificial molecular networks for precise identification and signal processing of biomolecules.[13] Therefore, artificial network circuits provide a powerful tool for studying complex physiological activities, information transfer, disease diagnosis, and efficient drug delivery.

The high predictability and programmability of DNA make it particularly suitable for building complex biological circuits to perform complex biological functions.[14–18] Particularly, as catalytic nucleic acids, DNAzymes can be integrated with other specific nucleic acid sequences and endowed with specific functions.[19–22] They hold great promise as transducing agents for the analysis of biomarkers *in vitro* or *in vivo*.[23–25] MicroRNAs (miRNAs), a class of short noncoding RNA molecules (18–22 nt), play significant regulatory roles in many physiological events.[26–28] By analysing the expression level of miRNAs in living cells, a wealth of information can be obtained to understand the relationship between miRNAs and the early diagnosis and treatment of tumors.[29,30] In the past few years, DNAzymes as transducing agents have been applied to develop efficient methods for detecting and visualizing endogenous miRNAs in living cells, especially for analysing the specific biological functions and effects of miRNAs on human health.[31,32] However, the wider application of these DNAzyme-based sensing platforms is limited by their inherent low catalytic efficiency and insufficient intracellular cofactors, which affect their amplification efficiency.[33–36] To improve the sensitivity of these sensing platforms for target molecule recognition, in recent years, researchers have combined DNAzyme-

State Key Laboratory for Organic Electronics and Information Displays & Jiangsu Key Laboratory for Biosensors, Institute of Advanced Materials (IAM), Jiangsu National Synergetic Innovation Center for Advanced Materials (SICAM), Nanjing University of Posts and Telecommunications, Nanjing 210023, P. R. China.
E-mail: iamjchao@njupt.edu.cn

† Electronic supplementary information (ESI) available. See DOI: https://doi.org/10.1039/d2nr05165f

catalyzed amplification methods with other non-enzymatic nucleic acid amplification methods, like the hybridization chain reaction (HCR), entropy-driven catalysis, and catalyzed hairpin assembly (CHA), to develop efficient amplification strategies for the identification of important intracellular biomolecules.[37–39] For example, Wang's group recently reported an intracellular miRNA imaging system based on a tandem CHA-HCR-DNAzyme circuit for miRNA detection.[40] In this system, the DNAzyme-catalyzed reaction was used as the final transduction element of the circuit. After the reaction was completed, there was no feedback to the superior CHA and HCR reactions, resulting in limited signal amplification ability for miRNA detection. Therefore, it is very important to design DNAzyme recycling circuits with efficient multistage cascade reactions. In addition to efficient signal amplification, the application in low-abundance biomarker analysis of DNAzyme circuits is limited by its low intracellular delivery efficiency and the need for an additional cofactor supply. To overcome this limitation, Ye's group designed an endogenous ATP-powered DNA motor for intracellular imaging.[41] This strategy provided a new way for DNA nanosystem operation in living cells powered by an auto-stimulus without auxiliary additives. In our previous study, we have reported DNAzyme–MnO_2 nanosystems for imaging miRNAs in living cells by target-triggered, self-powered DNAzyme-catalyzed reactions.[42,43] Recently, many CHA-DNAzyme circuits for intracellular microRNA imaging have been widely reported;[44–46] to address the problems of limited signal amplification capability and an additional supply of cofactors of DNAzyme-based bioassays, it is crucial to design a strategy that integrates DNAzyme biocircuits containing an intact feedback mechanism with nanomaterials that can provide catalytic capabilities.

Herein, we fabricated an intelligent, autocatalytic, DNAzyme biocircuit, enabling efficient imaging of intracellular miRNAs by triggering the coordinated cross-activation of CHA and autocatalytic DNAzymes. The DNAzyme biocircuits are constructed based on nanodevices composed of CHA and DNAzyme biocatalytic functional units, sustained by Au nanoparticles (AuNPs) and MnO_2 nanosheets (named CD/AM nanodevices). MnO_2 nanosheets can not only be used as nanocarriers for DNAzyme biocircuits, but also as cofactors for DNAzyme catalysts after reduction to Mn^{2+} by intracellular glutathione (GSH). As shown in Schemes 1A and B, the CD/AM nanodevice consists of hairpin DNA 1-modified AuNPs (H1-AuNPs), hairpin DNA 2 (H2), the double-stranded hybrid product of the substrate strand of Mn^{2+}-DNAzyme and the ligand strand (named S/L), and MnO_2 nanosheets. Once the nanodevice is endocytosed into living cells, H1-AuNPs, H2 and S/L are released following the degradation of MnO_2. In the presence of the target miRNA, the harpin structure of H1 conjugated on the AuNPs is opened and the fluorescence intensity of the fluorophore (Cy5) at the end of the H1 strand is restored as it moves away from the AuNPs. Subsequently, the H1-miRNA complexes react with H2 to generate H1–H2 complexes, one end of which assembles into a complete DNAzyme strand. Subsequently, the assembled DNAzyme strands combine with

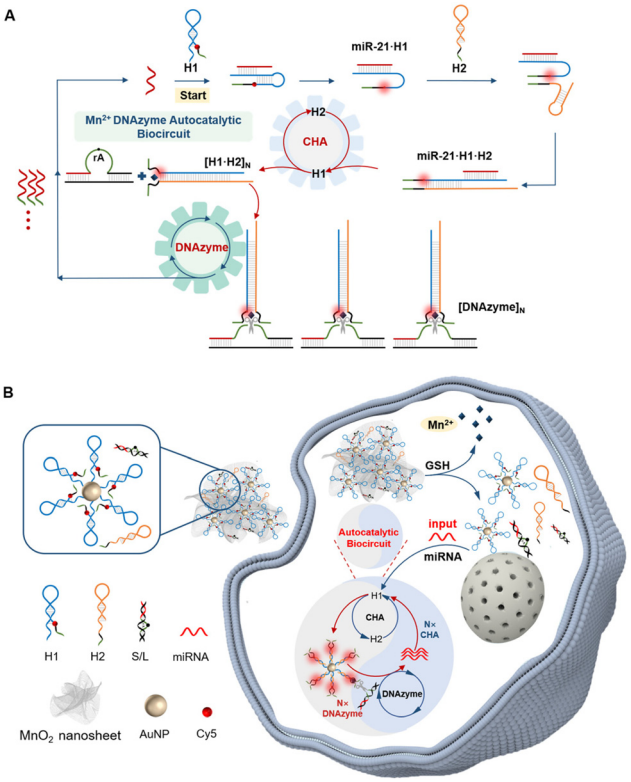

Scheme 1 Schematic illustrations of the CD/AM nanodevice for efficient imaging of intracellular miRNAs. (A) The coordinated cross-activation of CHA and autocatalytic DNAzymes by the target. (B) Schematic diagram of the CD/AM nanodevices for miRNA detection and imaging in living cells.

the substrate strand of S/L to form Mn^{2+}-DNAzyme. In the presence of Mn^{2+}, the substrate strand is cleaved into two parts, one of which could be fed back to the original CHA amplifier as a new trigger because it contains the same sequence as miRNA, resulting in the enhanced amplification of the fluorescence signal. The DNA catalytic units clustered on the surface of AuNPs increased the efficiency of the cross-reaction of CHA and autocatalytic DNAzymes and enhanced the *in situ* amplification signal for target detection. This system overcomes the limitations of low intracellular delivery efficiency and limited signal amplification capability (including an additional supply of cofactors) of DNAzyme biological circuits, enabling precise sensing and logical computing of intracellular biomolecules. Furthermore, this strategy could facilitate the application of smart DNAzyme biological circuits in biosensing, nanomaterial assembly, and biomedicine.

Experimental

Reagents and apparatus

All high-performance liquid chromatography (HPLC) purified oligonucleotides were provided by Sangon Biotechnology Co., Ltd (Shanghai, China) and their specific sequences are

described in the ESI Tables S1 and S2.† All hairpin DNA are heated at 95 °C for 10 min, and then cooled to room temperature, so that these probes are folded into hairpin structures. Four kinds of cells used in our experiments were purchased from KeyGEN Biotechnology Company (Nanjing, China). Additional reagents and instruments used in the experiments are detailed in the ESI.†

Preparation of MnO_2 nanosheets

We prepared MnO_2 nanosheets according to previous literature reports.[47] Firstly, a mixed solution (20 mL) containing 0.6 M tetramethylammonium hydroxide and 3 wt% H_2O_2 was added to 0.3 M $MnCl_2$ solution (10 mL) rapidly, and the mixture turned dark brown after stirring well for 20 s. Then, the solution was stirred overnight. The synthetic product was centrifuged at room temperature for 20 min at 2000 rpm and washed twice with water and methanol. After that, the supernatant was removed and the precipitate was vacuum dried at 60 °C. Finally, 10 mg of MnO_2 was weighed and dispersed with 20 mL of water, and MnO_2 nanosheets were obtained after ultrasonic treatment for 24 h.

Synthetic of H1-AuNPs

We prepared 25 nm AuNPs according to the classical synthetic route of citric acid.[48] H1 and H2 were separately rapidly annealed in 1× TAE Mg^{2+} buffer at 95 °C to ensure the formation of a hairpin structure. 10 μL of TCEP (1.0 mM) was added to H1 (1 μM) and diluted to 100 μL with phosphate buffered saline (PBS, pH = 7.4). After standing to react for 1 h, the solution was mixed with AuNP colloid (5 nM) and shaken overnight. The next day, 100 μL of mercapto polyethylene glycol (SH-PEG) solution was added to the above mixed solution and reacted in the dark for 10 h. To ensure the stability of the solution, 1 M NaCl was added to the mixed solution in multiple portions until the final concentration of NaCl was 0.1 M.

Preparation of CD/AM nanodevices

Firstly, the same amounts of single-stranded DNA (ssDNA) S strand and L strand were mixed and heated at 90 °C for 10 min. Then, the mixture was slowly annealed to room temperature to form a double-stranded DNA (dsDNA) structure S/L. After that, the H1-AuNP (50 μL, 5 nM), H2 (2 μL, 1 μM) and S/L (2 μL, 1 μM) solutions were mixed and added to MnO_2 nanosheet solutions (30 μL, 100 μg mL^{-1}); the above solutions were mixed and reacted for 1 h to form the CD/AM nanodevice.

In vitro fluorescence experiments

MiR-21 was selected as the analysis target in our experiments. Firstly, miRNA solutions at different concentrations (from 0 to 100 nM) were added to the CD/AM nanodevice solutions containing 2 mM GSH and incubated at 37 °C for 3 h. After that, the fluorescence spectra at 650–750 nm were recorded under the conditions of an excitation wavelength of 635 nm and a slit width of 5 nm, and the corresponding curves were obtained. Under the same experimental conditions, we tested the fluorescence responses of CD/AM nanodevices to various miR-21 analogues.

Gel electrophoresis experiments

Gel electrophoresis experiment was used to verify the reaction mechanism of the DNAzyme biocircuit for miRNA detection. Firstly, DNA markers (25–500 bp), H1 (10 μL, 1 μM), H2 (10 μL, 1 μM), S/L (10 μL, 1 μM), targeting miR-21 (10 μL,1 μM) and the corresponding reaction products were mixed with 2 μL of loading buffer, respectively. Then, samples were added to the corresponding lanes and polyacrylacetamide gel was run in 1× TBE buffer at 80 V for 30 min. Finally, the gel was stained with gel blue (5 min) for subsequent imaging on the Bio-Rad gel imaging system.

Cell culture

Four kinds of cells were used in our system. Human breast cancer cells (MCF-7 cells) and human normal mammary epithelial cells (MCF-10A cells) were cultured in the RPMI-1640 medium; the human hepatocellular liver carcinoma cell line (HepG2 cells) and human cervical cancer cells (HeLa cells) were cultured in the DMEM medium. All these media contain 10% fetal bovine serum (FBS) and 1% 1×10^4 per unit streptomycin/penicillin antibiotic solution. These cells were cultured in a 37 °C incubator with 5% CO_2.

Cell viability experiments

The biocompatibility of CD/AM nanodevices was evaluated by the MTT test method. At first, MCF-7 cells (150 μL) were seeded in 96-well plates at a density of 1×10^4 cells per well and cultured for 24 h. Next day, all cells were washed twice with PBS and then incubated with a serum-free 1640 medium containing 5 nM and 1 nM CD/AM nanodevices for 3 h, 6 h, 12 h, 18 h, and 24 h, respectively. After that, 20 μL of MTT (0.5 mg mL^{-1}) solution was added to the cell samples. The cells were incubated for 4 h to form formazan. The culture was terminated by carefully aspirating the medium from the wells. 150 μL of dimethyl sulfoxide (DMSO) was added to each well and 96-well plates were shaken at low speed for 10 min to fully dissolve the formazan crystals. The absorbance at 490 nm in each well was measured using a microwave reader, and the cell viability was evaluated.

miR-21 imaging in living cells

MCF-7 cells were seeded at a concentration of 2×10^5 cells per mL on 15 mm confocal laser dishes for 24 h. After that, the cells were incubated with 1 mL of DMRP 1640 medium containing CD/AM nanodevices (5 nM) for 3 h at 37 °C and further stained with nuclear dyes (Hoechst 33342) and lysosomal dyes (LysoTracker Green DND-26) to label nuclei and lysosome organelles. Finally, the cell samples were washed twice with PBS and imaged under a confocal microscope. Furthermore, the Cy5 fluorescence signals in MCF-7 cells, MCF-10A cells, HeLa cells and HepG2 cells were monitored

under the same experimental conditions. These images were analysed with the ImageJ software.

Results and discussion

Synthesis and characterization of the CD/AM nanodevices

The intelligent, autocatalytic DNAzyme biocircuits were constructed based on the CD/AM nanodevices consisting of H1-AuNPs, H2, S/L, and MnO_2 nanosheets. DNA motor–MnO_2 nanocomposites have been used for small molecule detection with distinct properties such as extraordinary stability in the cellular microenvironment, enhanced binding affinities to complementary DNA, ease of cell internalization, and resistance to degradation. MnO_2 nanosheets as nanocarriers in our system have many excellent properties, such as it can strongly adsorb ssDNA through physical adsorption, and could be reduced by GSH to form Mn^{2+}, which acted as the cofactor for DNAzymes. As shown in Fig. 1A, H1-AuNPs, H2, and S/L were designed to be absorbed on MnO_2 nanosheets by van der Waals forces and formed a complete nanodevice. Firstly, we used the transmission electron microscopy (TEM) and atomic force microscopy (AFM) analysis to verify the successful synthesis of CD/AM nanodevices. As the TEM images shown in Fig. 1B and C, the H1-AuNPs were uniformly dispersed and successfully adsorbed on the MnO_2 nanosheets (Fig. 1C). The AFM images showed that the prepared MnO_2 nanosheets exhibited an ultrathin sheet-like structure with a thickness of about 1 nm (Fig. 1D and E), and their diameters were distributed between 100–150 nm, which were further verified through dynamic light scattering (DLS) analysis (Fig. S1†). The degradation experiment of MnO_2 nanosheets *in vitro* verified that it could be well degraded by low content of GSH (Fig. S2†). Furthermore, the synthesis of the CD/AM nanodevices was also estimated by the UV-vis absorption spectroscopy and zeta potential analysis. As the UV-vis spectrometry results shown in Fig. S3,† compared with the bare AuNPs, the UV absorption peak of H1-AuNPs was red-shifted from 520 nm to 527 nm, and a characteristic deoxynucleotide absorption band appeared at 260 nm, which confirmed the modification of H1 on the surface of AuNPs. The characteristic absorption peak of MnO_2 appeared at 380 nm. An obvious slope change in the range of 300–500 nm and the absorption peaks at 525 nm and 260 nm were all occurred at the absorption spectrum of CD/AM nanodevices, which suggested the successful synthesis of the CD/AM nanodevices. Furthermore, the zeta potential analysis results given in Fig. 1F show that the CD/AM nanodevice had more negative potentials than H1-AuNPs and MnO_2, which further confirmed that the CD/AM nanodevice has been successfully fabricated.

Feasibility investigation of the CD/AM nanodevices for the detection of miRNA *in vitro*

Since miRNAs are highly expressed in cancer cells such as breast cancer and cervical cancer, they are often used as tumor markers for disease prevention and detection. As shown in Fig. 2A, in our system, the CD/AM nanodevices were designed for efficient detection of miRNAs *in vitro* or *in vivo* through the coordinated cross-activation of CHA and autocatalytic DNAzymes. In the presence of the target miRNA, the branch migration reaction of hairpin H1 was initiated by domain hybridization with the toehold domain of H1, resulting in the recovery of the Cy5 fluorescence signal for identifying miRNA. Then, the single-stranded toehold domain of the H1-miRNA

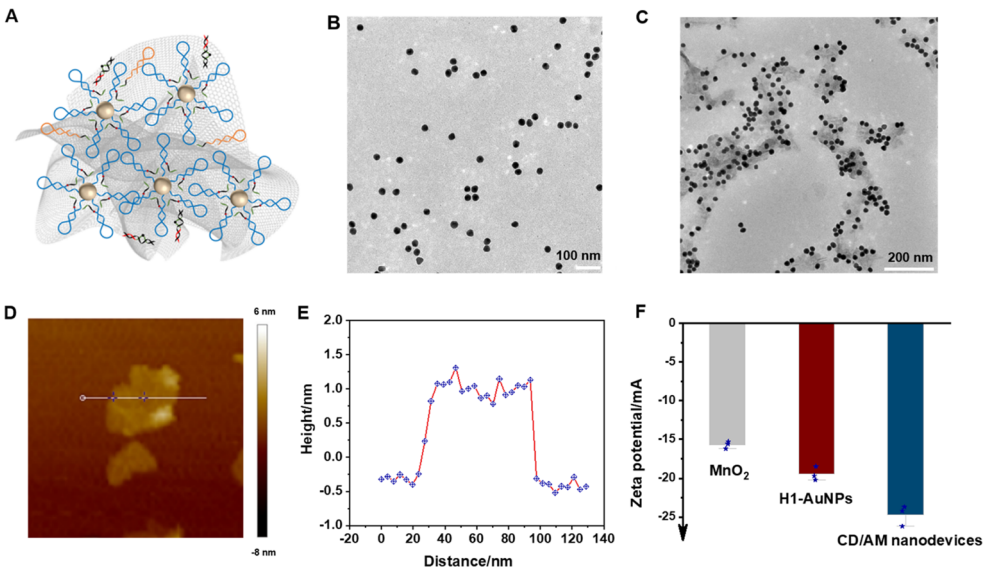

Fig. 1 Synthesis and characterization of CD/AM nanodevices. (A) Schematic illustration of the CD/AM nanodevice composed of H1-AuNPs, H2, S/L, and MnO_2 nanosheets. (B) and (C) TEM images of H1-AuNPs and CD/AM nanodevices. (D) AFM characterization of MnO_2 nanosheets. (E) The height image corresponding to the white line of MnO_2 nanosheets in (D). (F) Zeta-potential (ζ) values of MnO_2 nanosheets, H1-AuNPs and CD/AM nanodevices in PBS.

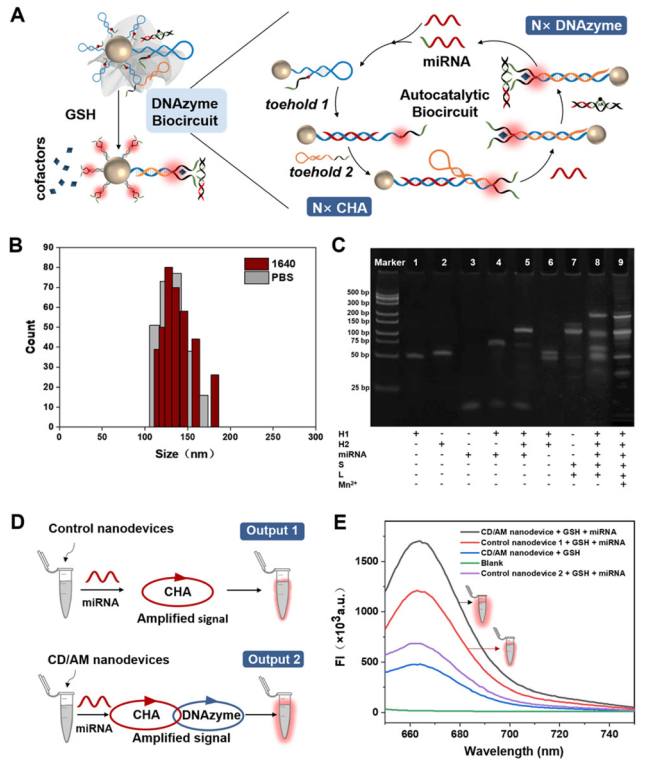

Fig. 2 Feasibility investigation of CD/AM nanodevices for the detection of miRNA *in vitro*. (A) Schematic diagram of the sensing mechanism of the CD/AM nanodevices to miR-21. (B) Stability of the CD/AM nanodevice in 1640 medium and PBS. (C) Gel electrophoresis characterization of the DNAzyme biocircuit for miRNA assay. (D) Schematic illustration of the fluorescence signal output of the CD/AM nanodevices and the control nanodevices for the *in vitro* detection of miRNA. (E) Fluorescence spectral responses of CD/AM nanodevices under different conditions.

intermediate further triggered another branch migration reaction of H2, resulting in the formation of the H1–H2 complexes, one end of which assembled into a complete Mn^{2+} DNAzyme strand. Subsequently, the assembled DNAzyme strands combined with the substrate strand of S/L to form Mn^{2+}-DNAzyme. In the presence of Mn^{2+}, as dsDNA S/L containing the restriction cleavage site rA in the substrate strand, the substrate strand was cleaved into two parts, one of which could be fed back as a new trigger to the original CHA amplifier because it contained the same sequence as intracellular miRNA, resulting in the enhanced amplification of the fluorescence signal. Therefore, in theory, the CD/AM nanodevices could achieve efficient detection of miRNAs by triggering the coordinated cross-activation of CHA and autocatalytic DNAzymes. The size of the CD/AM nanodevice in the 1640 complete culture medium and PBS verified the stability of the CD/AM nanodevice (Fig. 2B).

In our system, miR-21 was selected as the target for analysis due to its importance in the carcinogenesis and diagnosis of cancer. To demonstrate the feasibility of autocatalytic biocircuits based on the CD/AM nanodevices for miRNA detection, the polyacrylamide gel electrophoresis experiment and fluorescence spectrum experiments were performed. As shown in Fig. 2C, H1, H2, and miRNA had a good metastable state, corresponding to lane 1, lane 2, and lane 3, respectively. After H1 was incubated with miRNA, a new band with a larger molecular weight (lane 4 in Fig. 2C) was observed due to toehold-mediated hybridization reactions, which corresponded to the dsDNA products of H1 and miRNA. After the dsDNA products of H1 and miRNA continued to be incubated with H2, another new band with a large molecular weight appeared (lane 5 in Fig. 2C), which demonstrated that the H2 toehold could further react with H1-miRNA complexes and formed dsDNA H1–H2. In the absence of target miRNA, H1 and H2 could not undergo the CHA reaction and were two independent bands (lane 6, Fig. 2C). The dsDNA S/L had a larger molecular weight (lane 7 in Fig. 2C and lane 3 in Fig. S4†) than the single strand of S or L (lane 1 and lane 2 in Fig. S4†). Furthermore, the product of dsDNA H1–H2 with S/L in lane 8 suggested that while without the assistance of Mn^{2+}, a new DNA hybrid product of H1–H2 and S/L was generated for the subsequently DNAzyme-catalyzed reaction. The emerging band in lane 9 of the cleaved fragments of S–L demonstrated the high catalytic activity of the CHA-generated DNAzyme, which ensured the cross-reaction of CHA and autocatalytic DNAzymes of CD/AM nanodevices. These results indicated the occurrence of the CHA amplification reaction and the catalytic activity of the CHA-generated DNAzyme. Furthermore, the number of H1 loaded on each AuNP was calculated to be ~81 (Fig. S5A and S5B†), and the optimal ratios of H1 to H2 strands and H2 to S/L on MnO_2 nanosheets were observed at the ratios of 1 : 8 and 1 : 1 (Fig. S5C and S5D†).

After that, we further validated the sensing ability of the CD/AM nanodevices by a series of fluorescence experiments. Firstly, the control nanodevice 1 (without S/L) and control nanodevice 2 (without hairpin H2) were designed for investigating the coordinated cross-reaction of CHA and autocatalytic DNAzymes of the CD/AM nanodevices. In theory, the control nanodevices 1 only could active the CHA reaction in the presence of miRNA because they did not contain the substrate strand of the DNAzyme (Fig. 2D). This was further investigated by comparing the fluorescence signals caused by the control nanodevices 1 and the CD/AM nanodevices 2 in the presence of miRNAs. As the experimental results shown in Fig. 2E, the CD/AM nanodevice exhibited a strong fluorescence spectral response in the presence of 200 nM miRNA; however, a relatively weak signal was obtained with the control nanodevices 1 and 2 under the same conditions, indicating that the CD/AM nanodevices were able to recognize miRNAs and generate significantly enhanced fluorescence signals. While no target miRNA was added to the CD/AM nanodevice solution, an extremely low fluorescence signal was detected. We further conducted a series of fluorescence kinetic experiments to study the input and output responses. The kinetic tracer curve illustrated in Fig. S6† showed that the fluorescence signal significantly enhanced after the addition of the initiator miRNA, and gradually increased with the increase of the target concen-

tration, indicating that the execution of our cross-catalytic circuit depends on the input concentration of the target. This conclusion was consistent with previous research.[46] All these results suggested that the CD/AM nanodevice could be used for miRNA detection with amplified fluorescent signals by the coordinated cross-reaction of CHA and autocatalytic DNAzymes.

Analytical performance of CD/AM nanodevices for miRNA

To explore the sensitivity and selectivity of the CD/AM nanodevices for detecting miRNAs, the fluorescence spectra of CD/AM nanodevices were recorded in the presence of different concentrations of miR-21 (from 0 to 100 nM). In our design, miR-21 could trigger the coordinated cross-activation of CHA and autocatalytic DNAzymes of the CD/AM nanodevices and produce the corresponding fluorescence signal response (Fig. 3A). As the fluorescence spectrum results shown in Fig. S7† and Fig. 3B, in the presence of GSH (2 mM), the fluorescence intensity at 663 nm gradually increased with increasing miRNA concentration from 0 to 100 nM. Furthermore, the $F - F_0$ value (F and F_0 were the fluorescence intensities at 663 nm in the presence and absence of miRNA, respectively) was proportional to the miR-21 concentration and had a good linear correlation in the range of 0–5 nM (Fig. 3C). The detection limit was calculated as 0.1 pM based on traditional 3σ method, which was lower than that in the previous research.[49,50] These results evaluated the sensitivity of our strategy.

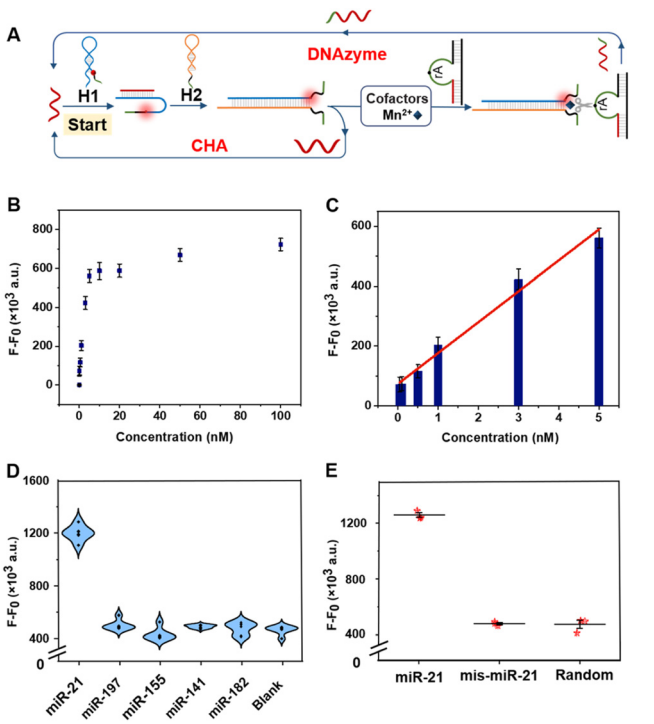

Fig. 3 Analysis of the detection performance of the CD/AM nanodevices for miRNA. (A) Schematic diagram of the principle of detecting miRNA. (B) Fluorescence spectral responses to different concentrations of miRNA (from 0 to 100 nM). (C) Calibration curve of $F - F_0$ *vs.* different concentrations of miRNA (from 0 to 5 nM). F and F_0 are the fluorescence intensities at 663 nm in the presence and absence of miRNA, respectively. (D) and (E) Specificity of the CD/AM nanodevice toward analogues from the miRNA family. Error bars were estimated from multiple replicate measurements.

After that, we further investigated the specificity of this system through detecting the fluorescence signal of the CD/AM nanodevices to various miRNA analogues. As shown in Fig. 3D, only an obvious fluorescent signal could be obtained in the presence of miR-21, while weak fluorescence signals were generated in the presence of other miRNAs such as miR-197, miR-155, miR-141 and miR-182. To more accurately demonstrate the specificity of our CD/AM nanodevice, we also tested the fluorescence signal of the CD/AM nanodevice to mis-miR-21 (which is a base mismatch DNA sequence of the original sequence of miR-21) and a random sequence to investigate whether our system could avoid a false-positive signal interference caused by multiple base mismatches. As the results shown in Fig. 3E, a strong fluorescence signal was observed in the presence of miR-21; however, almost no signal was observed in the presence of these mismatched targets. These experimental results indicated that our CD/AM nanodevices had excellent selectivity and specificity for detecting target miR-21, and can distinguish between the target analytes and sequences with multiple base mismatches.

In situ imaging analysis of intracellular targets

MCF-7 cells were selected as cell models to verify the performance of CD/AM nanodevices for the *in situ* imaging of intracellular targets. First, the biocompatibility of the CD/AM nanodevice was verified by MTT experiment. As shown in Fig. S8,† after MCF-7 cells were incubated with 1 nM and 5 nM nanodevices for 24 h, there was 80% of cells still maintained good cell viability. The experimental results showed that the CD/AM nanodevices had good biocompatibility for living cells and could not cause obvious side effects to cells. Moreover, we assessed the content of elemental Mn in living cells by inductively coupled plasma optical emission spectroscopy (ICP-OES) analysis; there was around 400 μM Mn element in the living cells after the cells were incubated with a 5 nM DNA CD/AM nanodevice for 3 h. The content of Mn element in living cells was enough to support rapid and autonomous operation of DNA motors in living cells as the DNAzyme motor reliably operated in the presence of 250–2000 μM Mn^{2+}.[51] After that, the ability of the CD/AM nanodevice to image intracellular miR-21 was evaluated by confocal fluorescence imaging experiments. MCF-7 cells were divided into four groups, the first and second groups were incubated with the CD/AM nanodevices and the control nanodevices 1 (without S/L) and 2 (without H2) for 3 h, and the fourth group was left untreated. As the fluorescence imaging results shown in Fig. 4A, obvious fluorescence intensity was observed in MCF-7 cells incubated with the CD/AM nanodevices and the control nanodevices 1 and 2, while no fluorescence intensity was observed in the blank control group. Furthermore, the fluorescence intensity of

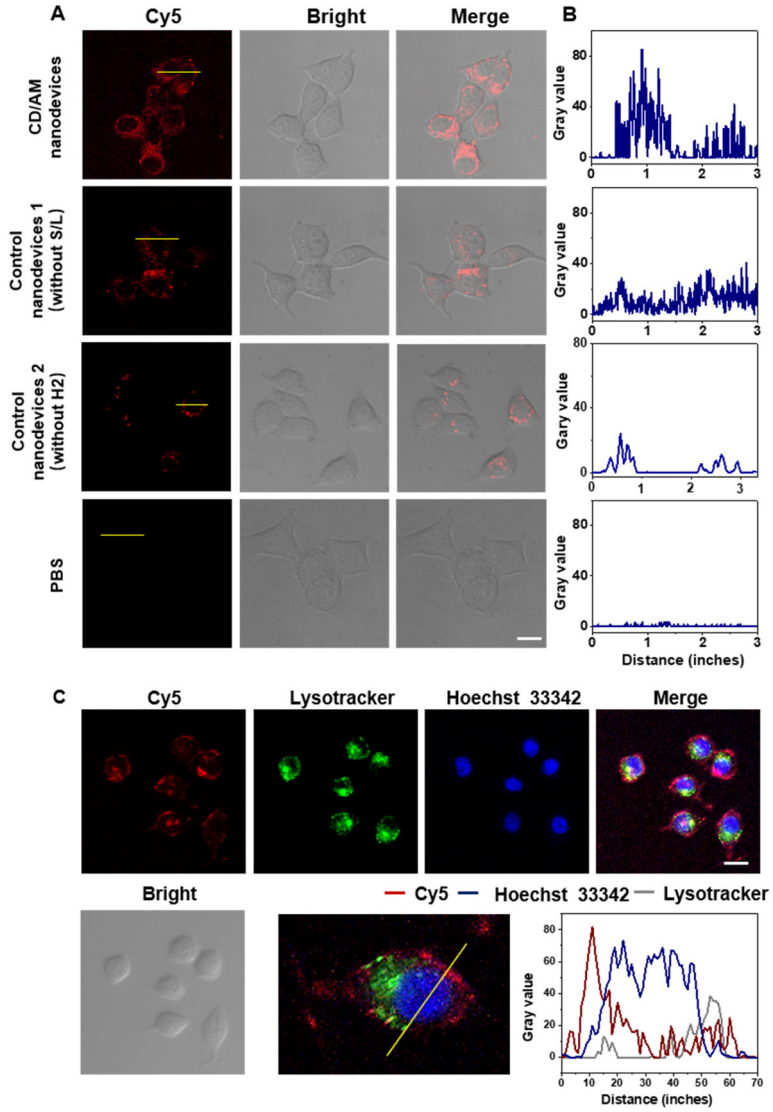

Fig. 4 The CD/AM nanodevices for imaging intracellular miRNA. (A) CLSM images of MCF-7 cells incubated with the CD/AM nanodevices, the control nanodevices, and PBS. Scale bar: 20 μm. (B) Quantification of the local fluorescence intensity of a single cell in (A). (C) The colocalization experiment images of the cells incubated with the CD/AM nanodevice, Hoechst 33342 and LysoTracker Green DND-26 and the quantification of the local fluorescence intensity of cells.

MCF-7 cells incubated with the CD/AM nanodevice was significantly stronger than that of cells incubated with the control nanodevices 1 and 2. Moreover, this result was consistent with that of single-cell fluorescence profile quantitative analysis (Fig. 4B). These results were due to the coordinated cross-activation of CHA and autocatalytic DNAzymes after the CD/AM nanodevice recognized intracellular miR-21, thus achieving obvious signal amplification. As shown in Fig. S9†, the fluorescence intensity in the Cy5 channel gradually increased with the increase of the incubation time from 1–3 h and there was basically no significant change at 4 h. These results indicated that 3 h was enough for intracellular miRNA to trigger the coordinated cross-activation of CHA and autocatalytic DNAzymes, which was chosen as the optimal incubation time.

Localization of intracellular imaging

After that, the distribution of target miRNAs in living cells was further explored by co-localization experiments with the acidic organelle-lysosome region (LysoTracker Green DND-26) dye and nuclei dye (Hoechst 33342) in MCF-7 cells. As the results shown in Fig. 4C, after cells were incubated with nanodevices, Lysotracker and Hoechst 33342, the red fluorescence signal from the CD/AM nanodevice mainly distributed in the cytoplasm and there was almost no overlap between the two channels of LysoTracker Green DND-26 and Cy5, which not only suggested that the CD/AM nanodevice could successfully escape from acidic organelles (endo/lysosome) into the cytoplasm, but also illustrated that miR-21 was mostly distributed in the cytoplasm.

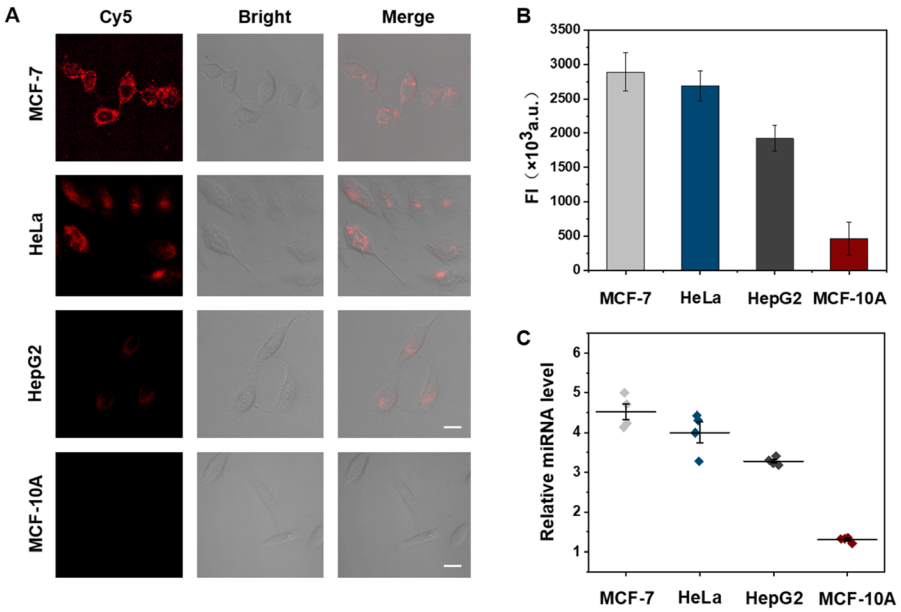

Fig. 5 The CD/AM nanodevice for imaging miRNA in living cells with different expression levels. (A) Confocal microscopy images of miR-21 in MCF-7 cells, HeLa cells, HepG2 cells and MCF-10A cells. Scale bar: 20 μm. (B) The total fluorescence intensity quantification of the four kinds of cells incubated with the CD/AM nanodevices. (C) qRT-PCR analysis of the expression of miR-21 in the above four cells. Error bars represent the standard deviation of four replicates.

Imaging miRNAs in different cells with the CD/AM nanodevices

The expression levels of the same miRNA in living cells were significantly different at the different stages of tumor development. Therefore, accurate imaging of miRNAs at different expression levels in living cells is very important for disease diagnosis and personalized therapy. Based on this, the ability of the CD/AM nanodevices was evaluated to image miRNA in different types of cells by the confocal microscopy imaging experiments. Specifically, MCF-7 cells, HeLa cells, HepG2 cells and MCF-10A cells were chosen as the four kinds of cell models. As the confocal images shown in Fig. 5A, after cells were incubated with the CD/AM nanodevices for 3 h, an obvious fluorescence signal was observed in MCF-7 cells and HeLa cells, and the fluorescence intensity was higher than that in HepG2 cells. The weakest fluorescence signal was observed in MCF-10A cells. These results were consistent with the total fluorescence intensity quantification results shown in Fig. 5B; miR-21 was most abundant in MCF-7 cells, followed by HeLa cells and HepG2 cells, and least abundant in MCF-10A cells. Furthermore, these results were further investigated by qRT-PCR analysis (Fig. 5C) and the results were in agreement with previous results.[52,53] These results suggested that the CD/AM nanodevice could be used for imaging intracellular miRNA with different expression levels.

Imaging multiple miRNAs in living cells

To investigate whether our designed intelligent, autocatalytic, DNAzyme biocircuit could be used for the amplified imaging of intracellular different miRNA sequences by adjusting the sequence of specific miRNA response parts, we designed a new nanodevice for the imaging of intracellular miR-155 (named as CD/AM nanodevice 155). The ability of this new nanodevice to image intracellular miR-155 was evaluated by confocal fluorescence imaging experiments. As the fluorescence imaging results shown in Fig. S10,† obvious fluorescence intensity was observed in MCF-7 cells incubated with the CD/AM nanodevices and the CD/AM nanodevice 155, while no fluorescence intensity was observed in the blank control group. The experimental results demonstrated the universality of our designed nanodevice for the detection of different miRNA families.

Conclusions

In summary, we successfully designed an intelligent, autocatalytic, DNAzyme biocircuit to perform the coordinated cross-reaction of CHA and autocatalytic DNAzymes, enabling precise sensing and logical calculation of intracellular biomolecules. In this system, the DNAzyme biocircuit was constructed based on a catalyzed CHA reaction and DNAzyme biocatalysis, sustained by AuNPs and MnO_2 nanosheets. The multifunctional MnO_2 nanosheets facilitated the cellular uptake of the nanodevices and could be degraded by intracellular GSH to achieve an adequate supply of DNAzyme cofactors. After miR-21 induced the CHA reaction, DNAzyme multimers were formed on AuNPs and could achieve *in situ* signal amplification. At the same time, DNAzyme autocatalysis generated a new trigger, which was fed back to the initial CHA reaction to realize the coordinated cross-activation and the cycle reaction of CHA and DNAzyme autocatalysis. The self-sufficiency of DNAzyme cofac-

tors improved its inherent low catalytic efficiency, and CHA mediation solved the problem of limited signal amplification of DNAzymes. The programmed delivery of stimuli-responsive nanodevices and the coordinated cross-activation of CHA and DNAzymes achieved precise localization and efficient imaging of intracellular miRNAs, facilitating the application of the intelligent DNAzyme biocircuit in biosensing, nanomaterial assembly, and biomedicine.

Author contributions

J. C. and M. R. C. conceived the project. M. R. C. and D. Z. designed and carried out the experiments. D. Z. and Q. F. W. collected and analyzed the data. J. C., M. R. C., D. Z. and Q. F. W. wrote the manuscript. All authors discussed the results and commented on the manuscript.

Conflicts of interest

There are no conflicts to declare.

Acknowledgements

This work was supported by the National Natural Science Foundation of China (21922408, 22274081, 62201288), the Natural Science Foundation of Jiangsu Province (BK20190038, BK20210585), the Science Foundation of Nanjing University of Posts and Telecommunications (NY220155), and the Key Program of Natural Science Research in Universities of Jiangsu Province (19KJA360007).

References

1 H. W. H. van Roekel, B. J. H. M. Rosier, L. H. H. Meijer, P. A. J. Hilbers, A. J. Markvoort, W. T. S. Huck and T. F. A. de Greef, *Chem. Soc. Rev.*, 2015, **44**, 7465–7483.
2 J. Li, P. Nowak and S. Otto, *J. Am. Chem. Soc.*, 2013, **135**, 9222–9239.
3 A. M. Feist, M. J. Herrgard, I. Thiele, J. L. Reed and B. O. Palsson, *Nat. Rev. Microbiol.*, 2009, **7**, 129–143.
4 U. S. Bhalla and R. Iyengar, *Science*, 1999, **283**, 381–387.
5 P. J. Conn, A. Christopoulos and C. W. Lindsley, *Nat. Rev. Drug Discovery*, 2009, **8**, 41–54.
6 A. P. Kornev and S. S. Taylor, *Trends Biochem. Sci.*, 2015, **40**, 628–647.
7 O. Dagliyan, N. V. Dokholyan and K. M. Hahn, *Nat. Protoc.*, 2019, **14**, 1863–1883.
8 Z. H. Foda, Y. Shan, E. T. Kim, D. E. Shaw and M. A. Seeliger, *Nat. Commun.*, 2015, **6**, 5939.
9 J. M. Lehn, *Chem. Soc. Rev.*, 2007, **36**, 151–160.
10 P. T. Corbett, J. Leclaire, L. Vial, K. R. West, J. L. Wietor, J. K. M. Sanders and S. Otto, *Chem. Rev.*, 2006, **106**, 3652–3711.
11 A. Herrmann, *Chem. Soc. Rev.*, 2014, **43**, 1899–1933.
12 S. Wang, L. Yue, Z. Y. Li, J. Zhang, H. Tian and I. Willner, *Angew. Chem., Int. Ed.*, 2018, **57**, 8105–8109.
13 A. Cangialosi, C. Yoon, J. Liu, Q. Huang, J. Guo, T. D. Nguyen, D. H. Gracias and R. Schulman, *Science*, 2017, **357**, 1126–1129.
14 P. Yin, H. M. T. Choi, C. R. Calvert and N. A. Pierce, *Nature*, 2008, **451**, 318–U314.
15 A. J. Genot, J. Bath and A. J. Turberfield, *J. Am. Chem. Soc.*, 2011, **133**, 20080–20083.
16 D. Y. Zhang, A. J. Turberfield, B. Yurke and E. Winfree, *Science*, 2007, **318**, 1121–1125.
17 M. Xiao, W. Lai, T. Man, B. Chang, L. Li, A. R. Chandrasekaran and H. Pei, *Chem. Rev.*, 2019, **119**, 11631–11717.
18 C. Chen, L. Zheng, F. Guo, Z. Fang and L. Qi, *Research*, 2021, **2021**, 1–10.
19 W. Zhou, Q. Chen, P. J. J. Huang, J. Ding and J. Liu, *Anal. Chem.*, 2015, **87**, 4001–4007.
20 H. Yin, H. Kuang, L. Liu, L. Xu, W. Ma, L. Wang and C. Xu, *ACS Appl. Mater. Interfaces*, 2014, **6**, 4752–4757.
21 X. Li, J. Xie, B. Jiang, R. Yuan and Y. Xiang, *ACS Appl. Mater. Interfaces*, 2017, **9**, 5733–5738.
22 T. Li, S. Dong and E. Wang, *Anal. Chem.*, 2009, **81**, 2144–2149.
23 P. J. J. Huang, J. Lin, J. Cao, M. Vazin and J. Liu, *Anal. Chem.*, 2014, **86**, 1816–1821.
24 T. T. Zhai, D. Ye, Y. Shi, Q. W. Zhang, X. Qin, C. Wang and X. H. Xia, *ACS Appl. Mater. Interfaces*, 2018, **10**, 33966–33975.
25 C. Yang, X. Yin, S. Y. Huan, L. Chen, X. X. Hu, M. Y. Xiong, K. Chen and X. B. Zhang, *Anal. Chem.*, 2018, **90**, 3118–3123.
26 R. A. Boon, K. Iekushi, S. Lechner, T. Seeger, A. Fischer, S. Heydt, D. Kaluza, K. Treguer, G. Carmona, A. Bonauer, A. J. G. Horrevoets, N. Didier, Z. Girmatsion, P. Biliczki, J. R. Ehrlich, H. A. Katus, O. J. Mueller, M. Potente, A. M. Zeiher, H. Hermeking and S. Dimmeler, *Nature*, 2013, **495**, 107–110.
27 Z. He, S. Peng, Q. Wei, S. Jia, S. Guo, K. Chen and X. Zhou, *CCS Chem.*, 2020, **2**, 89–97.
28 C. Chen, J. Wang, D. Lu, R. You, Q. She, J. Chen, S. Feng and Y. Lu, *Nanoscale*, 2022, **14**, 8103–8111.
29 J. R. Buchan and R. Parker, *Science*, 2007, **318**, 1877–1878.
30 P. Li, M. Wei, F. Zhang, J. Su, W. Wei, Y. Zhang and S. Liu, *ACS Appl. Mater. Interfaces*, 2018, **10**, 43405–43410.
31 D. He, X. He, X. Yang and H. W. Li, *Chem. Sci.*, 2017, **8**, 2832–2840.
32 Y. Zhou, M. Yu, C. Tie, Y. Deng, J. Wang, Y. Yi, F. Zhang, C. Huang, H. Zheng, L. Mei and M. Wu, *Research*, 2021, **2021**, 1–15.
33 R. R. Breaker and G. F. Joyce, *Chem. Biol.*, 1995, **2**, 655–660.
34 M. J. Cromie, Y. X. Shi, T. Latifi and E. A. Groisman, *Cell*, 2006, **125**, 71–84.
35 Y. Suzuki, H. Komatsu, T. Ikeda, N. Saito, S. Araki, D. Citterio, H. Hisamoto, Y. Kitamura, T. Kubota,

J. Nakagawa, K. Oka and K. Suzuki, *Anal. Chem.*, 2002, **74**, 1423–1428.
36 W. Zhou, Y. Zhang, J. Ding and J. Liu, *ACS Sens.*, 2016, **1**, 600–606.
37 F. Wang, J. Elbaz, R. Orbach, N. Magen and I. Willner, *J. Am. Chem. Soc.*, 2011, **133**, 17149–17151.
38 X. Tan, Q. Chen, H. Zhu, S. Zhu, Y. Gong, X. Wu, Y. C. Chen, X. Li, M. W. H. Li, W. Liu and X. Fan, *ACS Sens.*, 2020, **5**, 110–117.
39 Q. Wu, H. Wang, K. Gong, J. Shang, X. Liu and F. Wang, *Anal. Chem.*, 2019, **91**, 10172–10179.
40 H. Wang, H. Wang, Q. Wu, M. Liang, X. Liu and F. Wang, *Chem. Sci.*, 2019, **10**, 9597–9604.
41 P. Q. Ma, C. P. Liang, H. H. Zhang, B. C. Yin and B. C. Ye, *Chem. Sci.*, 2018, **9**, 3299–3304.
42 M. R. Cui, X. L. Li, J. J. Xu and H. Y. Chen, *Chem. Commun.*, 2019, **55**, 13366–13369.
43 M. R. Cui, X. L. Li, H. Y. Chen and J. J. Xu, *CCS Chem.*, 2021, **3**, 2063–2073.
44 Y. Wan, G. Li, L. Zou, H. Wang, Q. Wang, K. Tan, X. Liu and F. Wang, *Anal. Chem.*, 2021, **93**, 11052–11059.
45 X. Gong, R. Li, J. Wang, J. Wei, K. Ma, X. Liu and F. Wang, *Angew. Chem., Int. Ed.*, 2020, **59**, 21648–21655.
46 L. Zou, Q. Wu, Y. Zhou, X. Gong, X. Liu and F. Wang, *Chem. Commun.*, 2019, **55**, 6519–6522.
47 H. Fan, Z. Zhao, G. Yan, X. Zhang, C. Yang, H. Meng, Z. Chen, H. Liu and W. Tan, *Angew. Chem., Int. Ed.*, 2015, **54**, 4801–4805.
48 H. Peng, X. F. Li, H. Zhang and X. C. Le, *Nat. Commun.*, 2017, **8**, 14378.
49 J. Liu, M. R. Cui, H. Zhou and W. Yang, *ACS Sens.*, 2017, **2**, 1847–1853.
50 M. R. Cui, Y. Chen, D. Zhu and J. Chao, *Anal. Chem.*, 2022, **94**, 10874–10884.
51 H. Peng, X.-F. Li, H. Zhang and X. C. Le, *Nat. Commun.*, 2017, **8**, 14378.
52 Y. Wu, J. Huang, X. Yang, Y. Yang, K. Quan, N. Xie, J. Li, C. Ma and K. Wang, *Anal. Chem.*, 2017, **89**, 8377–8383.
53 Z. Cheglakov, T. M. Cronin, C. He and Y. Weizmann, *J. Am. Chem. Soc.*, 2015, **137**, 6116–6119.